Electronic Supplementary Information for

Water Self-dissociation in Slit Pores Displays Non-monotonic Behavior as a Function of Water Filling

Sergi Ruiz-Barragan*[a], Daniel Muñoz-Santiburcio[b], Saskia Körning[c], Dominik Marx[c]
[a] *Universitat Politécnica de Catalunya, Departament de Fisica, Rambla Sant Nebridi 22, Terrassa 08222, Barcelona, Spain; email: sergio.ruiz.barragan@upc.edu*
[b] *Instituto Andaluz de Ciencias de la Tierra (IACT-CSIC), Spanish Research Council, Av. de las Palmeras 4, 18100 Armilla, Spain*
[c] *Lehrstuhl für Theoretische Chemie, Ruhr-Universität Bochum, 44780 Bochum, Germany; e-mail: sergi.ruiz@theochem.rub.de*
(Dated: February 27, 2026)

CONTENTS

I. COMPUTATIONAL APPROACH

A. Simulation Details

The present study is based on *ab initio* molecular dynamics (AIMD) simulations [1]. All simulations in this work were performed using `CP2K` package [2–6], employing overall settings that we have introduced and validated in recent studies of water/graphene systems [7–10]. In particular, the electronic structure of the slit pore systems was treated using the RPBE [11] exchange-correlation functional supplemented by the D3 dispersion correction [12] (including as usual the two-body terms subject to zero damping). Here, all atoms in these inhomogeneous systems, notably including all carbons of the two graphene sheets, were explicitly treated at the quantum-mechanical level using GTH pseudopotentials [13–15], TZV2P basis sets [2] for oxygen and hydrogen atoms, and the TZV2P-MOLOPT basis [16] for the carbon atoms, in conjunction with a 500 Ry cutoff for the auxiliary planewave basis set that represents the valence electron density.

The AIMD simulations were performed with the Born–Oppenheimer propagation scheme [1] while employing a 0.4 fs timestep. Sampling the canonical (NVT) ensemble at $T = 300$ K was established using a Nosé–Hoover chain thermostat with a chain length of three. For the present slit pore simulations, see below for their setup, the normal (perpendicular) pressure was established and controlled by the rigid piston approach [17], as summarized in the following section I D, subject to the proper intrinsic density correction [8, 17] as determined earlier specifically for RPBE-D3. The parallel pressure is not controlled but evaluated using the effective anisotropic pressure approach as introduced and validated recently [18], see also section I D for background. For the bulk water reference RPBE-D3 NVT AIMD simulations, we used the density corresponding to 300 K and 1 bar according to the experimental equation of state [19], thus employing a cubic supercell with $a = 15.6627$ Å containing 128 H_2O molecules. The free energy profiles for water self-dissociation are calculated following the well-established thermodynamic integration approach, see section I C for details.

The set of NVT simulations for given constraint values as required to compute these free energy profiles, see section I C, were equilibrated for at least 5 ps before starting the production runs. In total, about 10 ns of full AIMD simulations after equilibration have been carried out to compute the five free energy profiles for water self-dissociation in slit pores and the respective free energy barriers as reported in this study.

B. Slit Pore Models

The specific nanoconfinements used in this work, based on fully atomistic graphene sheets that are seamlessly included in the all-QM treatment, have been designed by filling graphene-based slit pores with different numbers of water molecules in a usual periodic slab setup. The different slit pore setups are characterized by the interlayer distance (d_{int}) between the two coplanar graphene sheets (which might either fluctuate w.r.t. an average value in case of rigid piston simulations at controlled normal pressure or be fixed for frozen piston simulations as detailed in section I D) together with the area (or surface) number density (reported as $H_2O/Å^2$) defined as the total number of water molecules in the lamella divided by the surface area provided by the two identical graphene walls. This variable quantifies the water filling of the different slit pores independently of their in-plane lattice constants (a,b) of the periodic supercell and has been shown to provide a consistent measure for comparing different slit pore fillings [18].

Specifically in our simulations, the graphene sheets used contain 112 carbon atoms each, providing xy-lattice constants of $a = 17.12$ Å and $b = 17.30$ Å as determined previously specifically for the RPBE-D3 functional to be consistent [7]. The perpendicular c lattice constant along z was chosen to leave approximately 15 Å of vacuum between the periodic images along the surface normal in each case. The filling of the slit pores goes from 27 water molecules in the lamella (corresponding to a water filling of 0.091 $H_2O/Å^2$) up to 80 (providing an area number density of 0.270 $H_2O/Å^2$) as compiled in table S1 for the systems simulated (see also figure 1 of the main text).

For each slit pore setup, we performed rigid piston simulations [8, 17] (see section I D) to compute the equilibrium interlayer distance $\langle d_{\mathrm{int}} \rangle$ depending on water filling at 300 K while applying a normal pressure of 1 bar. As reviewed in section I D, this requires one to apply a perpendicular pressure of 1.6 kbar on the moving rigid piston as determined in previous work [8] to establish the intrinsic density correction corresponding to RPBE-D3 in order to reproduce the experimental density of bulk water at 300 K and 1 bar conditions in AIMD simulations of RPBE-D3 water thermostatted at 300 K. The AIMD sampling times of these rigid piston runs vary from 80 to 110 ps as required to converge the average value of the fluctuating interlayer distance $d_{\mathrm{int}}(t)$ for a given water filling of the slit pore; these $\langle d_{\mathrm{int}} \rangle$ values are used to fix the interlayer distances depending on water filling in the subsequent frozen piston simulations, see below. The resulting equilibrium interlayer distances are also reported in table S1, see also figure 1 of the main text. These average values are used to fix the interlayer distances for the frozen piston simulations which

are used to carry out the thermodynamic simulation runs to compute the free energy profiles (see section I C) and the effective parallel pressures required to quantify the anisotropy of the effective pressure tensor (see section I D).

Table S1. Number of H_2O molecules (N_{H_2O}) and corresponding area number density ($H_2O/Å^2$) for each of the graphene slit pores studied with in–plane (xy) lattice constants of $a = 17.12$ Å and $b = 17.30$ Å. The equilibrium interlayer distances ($\langle d_{int} \rangle$ as presented in figure 1 of the main text as a function of water filling) have been determined using rigid piston simulations (see text) to be subsequently used to setup the frozen piston simulations (see text) where the interlayer distance of the slit pores has been fixed to compute properties.

N_{H_2O}	$H_2O/Å^2$	$\langle d_{int} \rangle$ (Å)
27	0.091	6.69
33	0.111	6.87
34	0.115	6.98
35	0.118	7.37
39	0.132	8.28
40	0.135	8.50
45	0.152	9.02
49	0.165	9.25
54	0.182	9.42
59	0.199	9.54
62	0.209	9.57
63	0.212	9.62
64	0.216	9.67
65	0.219	10.18
70	0.236	11.12
80	0.270	12.28
105	0.354	14.69

C. Thermodynamic Integration Simulations

The free energy profiles of the water self-dissociation reaction at the different conditions and environments were determined as usual from thermodynamic integration within the "Blue Moon" ensemble [20, 21] as summarized in section 3.7.3 of Ref. [1]. In this well-known approach, the process of interest is simulated step-wise by generating a set of simulation replica where a given collective variable is constrained to different values. To study the free energy for water self-dissociation [22], the collective variable employed is the coordination number $CN_{O^*,H}$ of a given oxygen atom O^* with respect to all hydrogen atoms, which when constrained progressively from $CN_{O^*,H} \approx 2$ to $CN_{O^*,H} \approx 1$ effectively enforces the dissociation of that water molecule,

$$CN_{O^*,H} = \sum_i \frac{1 - \left(\frac{r_{O^*H_i}}{r_0}\right)^a}{1 - \left(\frac{r_{O^*H_i}}{r_0}\right)^b} \quad , \tag{1.1}$$

where i runs over all hydrogen atoms in the system; the parameters $a = 10$, $b = 28$, and $r_0 = 1.44183$ Å were chosen to reproduce the shape of the coordination number function [23].

The free energy profile of water self-dissociation along the $CN_{O^*,H}$ variable, $\Delta F(CN_{O^*,H})$, is readily obtained from the average forces of constraint which in turn are obtained from the corresponding Lagrange multipliers subject to additional geometric corrections defined below, $\langle f(CN'_{O^*,H}) \rangle$, computed at a set of fixed values of $CN_{O^*,H}$ based on using constrained reaction coordinate dynamics [20] of these replica. These average forces are computed from

$$\langle f(CN'_{O^*,H}) \rangle = \frac{\langle Z^{-1/2}[\lambda - k_B T G] \rangle_{CN'_{O^*,H}}}{\langle Z^{-1/2} \rangle_{CN'_{O^*,H}}} \quad , \tag{1.2}$$

where $CN'_{O^*,H}$ denotes the specific value of the coordination number constraint in that run, λ is the Lagrange multiplier

associated to the constraint, and Z as well as G are defined [21] as

$$Z = \sum_{i}^{N} \frac{1}{m_i} \left(\frac{\partial \mathrm{CN}_{\mathrm{O}^*,\mathrm{H}}}{\partial \mathbf{r}_i} \right)^2 \quad , \tag{1.3}$$

$$G = \frac{1}{Z^2} \sum_{i,j}^{N} \frac{1}{m_i m_j} \frac{\partial \mathrm{CN}_{\mathrm{O}^*,\mathrm{H}}}{\partial \mathbf{r}_i} \frac{\partial^2 \mathrm{CN}_{\mathrm{O}^*,\mathrm{H}}}{\partial \mathbf{r}_i \partial \mathbf{r}_j} \frac{\partial \mathrm{CN}_{\mathrm{O}^*,\mathrm{H}}}{\partial \mathbf{r}_j} \quad , \tag{1.4}$$

where i, j run over all atoms involved in the definition of the collective variable $\mathrm{CN}_{\mathrm{O}^*,\mathrm{H}}$. Using the free energy profiles, $\Delta F(\mathrm{CN}_{\mathrm{O}^*,\mathrm{H}})$ (shown below in Fig. S3), the value at $\mathrm{CN}_{\mathrm{O}^*,\mathrm{H}} = 1.3$ is used to determine the free energy of water self-dissociation.

D. Slit Pore Pressure: Piston Approaches, Effective Pressure Calculations, and Intrinsic Density Correction

The piston approach [17] has been used to control the normal (perpendicular) pressure in slit pore systems. This approach has been comprehensively validated in our previous works using both, computationally efficient force field molecular dynamics [17, 18] and *ab initio* molecular dynamics [8] based on the RPBE-D3 density functional as used in the present work.

Specifically, we use here the rigid piston approach for our set of slit pore models, see table S1 for the details. In rigid piston simulations, a fixed normal pressure is applied to the system through the confining media, in this case the graphene sheets, via forces acting on the atoms of the confining walls (carbon atoms here) that are restricted to remain within the same plane according to the ideal hexagonal lattice structure of graphene along the AIMD simulations (which we call rigid piston, whereas in the flexible piston method the graphene walls are not rigid but fully dynamical as assessed previously [17]). The walls can move along the normal axis, thus the interlayer distance (d_{int}) fluctuates along each simulation around some mean which defines in equilibrium its average value ($\langle d_{\mathrm{int}} \rangle$) upon convergence as reported in table S1 for all slit pore models.

In order to more efficiently converge properties of the different slit pore setups depending on water filling, we use the frozen piston approach where the interlayer distance is fixed. As we have shown earlier [17], using such frozen piston simulations where the interlayer distance has been fixed according to the average value $\langle d_{\mathrm{int}} \rangle$ as determined from the corresponding rigid piston simulation yield essentially indistinguishable results. Moreover, we have shown that the effective perpendicular pressure generated in the slit pores is the same as the normal pressure that is applied to the rigid piston as described above [18]. For this reason, we used the frozen piston methodology with the consistent interlayer distances $\langle d_{\mathrm{int}} \rangle$ corresponding to the water fillings in order to compute the free energy profiles for water self-dissociation as well as the effective parallel pressures for the different nanoscale environments that we studied.

Concerning the calculation of the anisotropic pressure inside the slit pores, we used the effective pressure approach [18] as a validated practical method to obtain the parallel and perpendicular components of an effective pressure tensor for an inhomogeneous fluid confined inside a slit pore with coplanar and fixed confining walls, i.e. corresponding to frozen piston simulations. Here, we transfer the same methodology as introduced before in the realm of force field simulations of water in slit pores [18] to the corresponding frozen piston AIMD setup described above. The obtained values of $\mathbf{P}_{\parallel}^{\mathrm{eff}}$ are shown in Fig. S4, while the values of $\mathbf{P}_{\perp}^{\mathrm{eff}}$ are by construction equal to the normal pressure used in the rigid piston simulations that defined the corresponding $\langle d_{\mathrm{int}} \rangle$ values.

In addition to taking into account the pressure anisotropy in the case of inhomogeneous liquids, it is also crucial to consider the intrinsic density correction [8, 17] which is necessary for slit pore simulations if referenced to bulk water simulations at experimental thermodynamic conditions for the following reason. In bulk water AIMD simulations, one typically uses the experimental equation of state to determine the volume for NVT simulations via the cubic box length of the periodic supercell (according to the density at the desired temperature and pressure conditions, here 300 K and 1 bar) as also done in the present study. However, the intrinsic density computed from NpT simulations, thus corresponding to the experimental isobaric-isothermal conditions, is typically different from the experimental density. This problem not only applies to force fields but it is known since long that this is also relevant to density functionals which might both under- and overestimate the experimental density at a given thermodynamic state point in NpT AIMD simulations [24, 25]. We determined this effect specifically for the RPBE-D3 functional and quantified the underestimation of the mass density at 1 bar and 300 K conditions [8]. This effect is only a problem in constant pressure simulations since in constant volume simulations of bulk liquids the volume can be easily adjusted as to produce the correct experimental density, which is the common approach as just mentioned. However, rigid piston simulations are constant normal pressure simulations and, thus, suffer from this artifact when comparing

water properties obtained under anisotropic confinement conditions, e.g. in slit pores, to the same properties in the isotropic reference system, i.e. in bulk water. As a correction to this systematic deviation, we introduced in previous works [8, 17] the intrinsic density correction. It implies applying an additional pressure during constant pressure simulations to correct for the density difference, which can be applied to any pressure control such as usual barostats or the piston approach. For RPBE-D3, we have previously determined [8] that applying an excess pressure of 1.6 kbar adjusts for the underestimated density of water at 300 K, which we apply here to the constant normal pressure in our rigid piston AIMD simulations to establish an effective perpendicular pressure of 1 bar inside the slit pore at 300 K.

II. SUPPORTING COMPUTATIONAL ANALYSES

A. Validation of Activation Free Energy Calculations

We scrutinized whether the employed overall methodology appropriately captures the free energetics of the self-dissociation reaction in the bulk water regime and, in particular, whether it is robust with respect to changes of thermodynamic conditions. Since the self-dissociation free energy barrier of bulk water is more sensitive to temperature than pressure changes, we validated our computational method by benchmarking the calculated barriers versus experimental data upon varying the temperature.

To that end, we computed from RPBE-D3 NVT AIMD simulation using 32 H_2O molecules the ΔF profiles at different temperatures from 300 to 500 K at the experimental densities corresponding to each temperature at 0.2 kbar according to the accurate equation of state of water [19], which probes a significant change of density from 1005.3 to 846.5 kg/m^3. The resulting ΔF profiles (Fig. S1) show that the current approach nicely captures the changes of the activation free energy to water dissociation upon changing the density and temperature conditions. Although the agreement of the computed temperature response of the activation free energy (inset of Fig. S1) obtained from RPBE-D3 is very convincing compared to the experimental reference data [26], we note that we are not focusing on reproducing the absolute values of the activation free energies at these different conditions but the trend depending on density changes.

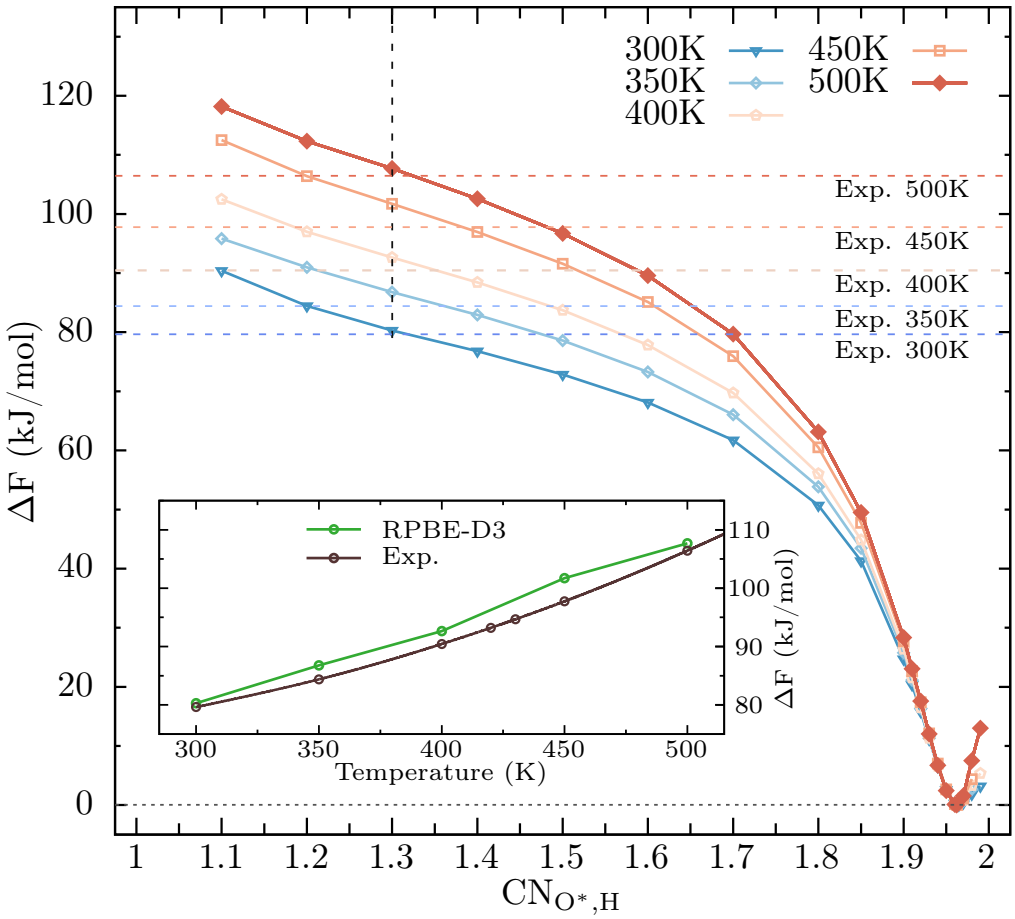

Figure S1. Free energy profiles computed for the H_2O self-dissociation reaction in liquid water relative to the reactant state for bulk water at 0.2 kbar and different temperatures from 300 K to 500 K (see text) obtained from RPBE-D3 NVT AIMD simulations in comparison to the experimental values [26] at the same thermodynamic conditions (horizontal dashed lines). The inset shows the relative activation free energy for this reaction (estimated from ΔF at $CN_{O*,H} = 1.3$) as a function of temperature in comparison to the experimental values.

B. Assessing Finite-size Effects on Free Energy Profiles

Since the reference bulk water system against which we compared the results of the different slit pores in Fig. 1 of the main text (or Fig.S3 here) contained 128 H_2O molecules, as opposed to quantities between 45 and 64 molecules in the case of the slits, we carried out additional simulations to assess any possible size effects. To that aim, we compared the results of the 128 H_2O bulk water system at the experimental density corresponding to 300 K and 1 bar to a 32 H_2O bulk water system at the same density. The results, in Fig. S2, make clear that the presence of size effects from using 128 down to 32 H_2O molecules is in practice negligible.

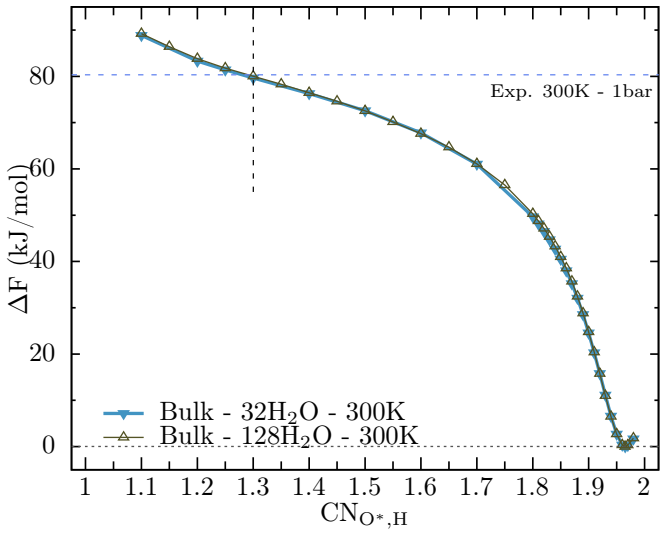

Figure S2. Free energy profile for water self-dissociation in bulk water at 300 K and 1 bar obtained from RPBE-D3 NVT AIMD simulations using two different system sizes of 32 and 128 water molecules in a periodic cubic supercell yielding the experimental density at this thermodynamic state point.

C. Free Energy Profiles for Water Self-dissociation in Slit Pores

As explained in the manuscript, using the methodology of section I C, we calculated the free energy profile for water self-dissociation for bulk water and for five different graphene slit pores with different water fillings depicted in Fig. S3 to extract the self-dissociation free energies that are shown in figure 2 of the main text. In total, about 10 ns of full AIMD simulations after equilibration have been carried out to compute these five free energy profiles for water self-dissociation in slit pores and the respective free energy barriers as reported in this study.

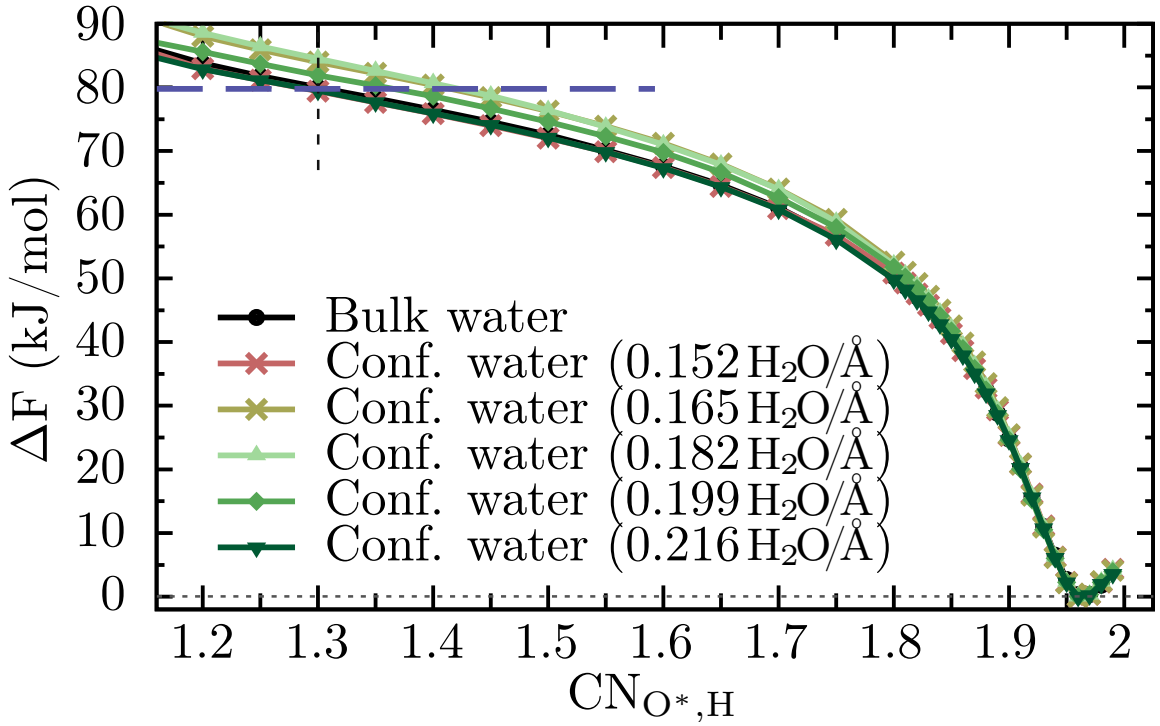

Figure S3. Free energy profiles for water self-dissociation of bilayer water at 300 K confined in graphene slit pores at a perpendicular pressure corresponding to 1 bar at 300 K (thus at constant excess piston pressure of 1.6 kbar to consider the intrinsic density correction, see text) at the corresponding fixed equilibrium interlayer distances, d_{int}, as a function of pore filling, $H_2O/Å^2$ obtained from thermodynamic integration, see text. For reference, the free energy profile corresponding to isotropic bulk water at 1 bar and 300 K (thus at constant excess pressure of 1.6 kbar to consider the intrinsic density correction, see text) is included. The symbols mark the fixed coordination numbers $CN_{O^*,H}$ for thermodynamic integration at which the underlying average forces have been computed from equation (1.2) to yield the depicted free energy profiles $\Delta F(CN_{O^*,H})$.

D. Effective Parallel Pressure for Slit Pore Setups

The effective parallel pressures of the five different slit pore setups (I) to (V) used in this work are calculated using the approach introduced in reference [18] as reviewed in section I D. The resulting values show a similar behavior with respect to what we observed earlier [18] for confined force field water: Negative pressures with a big increment when the water filling of the slit pore is near to inducing the structural transition from the bilayer to the trilayer stratification regime.

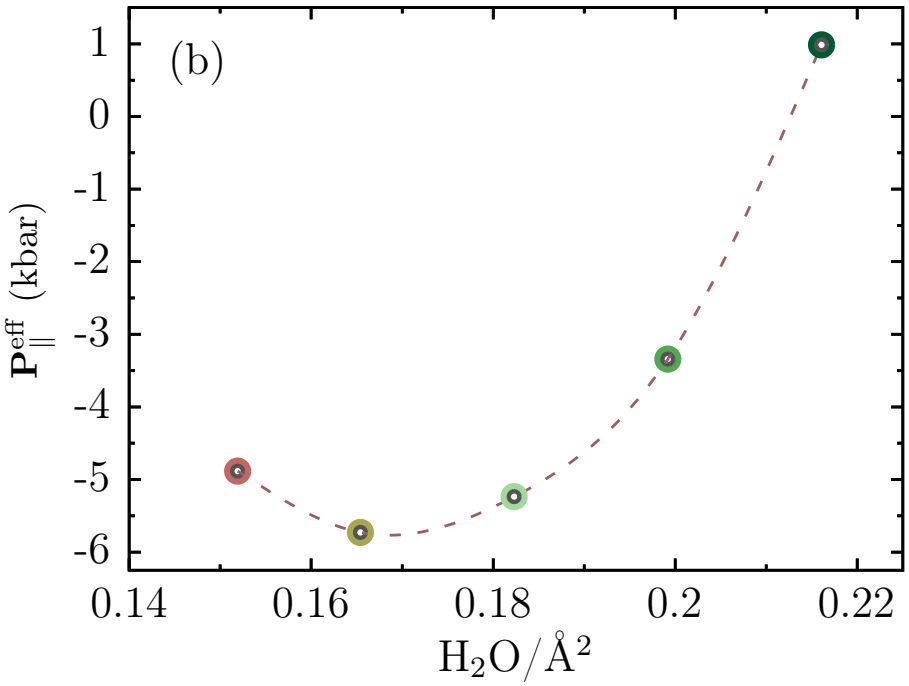

Figure S4. Effective parallel pressure, $\mathbf{P}_{\parallel}^{\mathrm{eff}}$, as a function of pore filling, $H_2O/Å^2$, for our graphene slit pore setups (I) to (V) at the corresponding fixed equilibrium interlayer distances, d_{int}, obtained with the rigid piston approach at a perpendicular pressure of 1.6 kbar to consider the intrinsic density correction as explained in section I D. The interpolating dashed line is a fit of the computed data points to guide the eye.

[1] D. Marx and J. Hutter, *Ab Initio Molecular Dynamics: Basic Theory and Advanced Methods* (Cambridge University Press, 2009).
[2] J. VandeVondele, M. Krack, F. Mohamed, M. Parrinello, T. Chassaing, and J. Hutter, Comput. Phys. Commun. **167**, 103 (2005).
[3] J. Hutter, M. Iannuzzi, F. Schiffmann, and J. VandeVondele, Wiley Interdiscip. Rev. Comput. Mol. Sci. **4**, 15 (2014).
[4] T. D. Kühne, M. Iannuzzi, M. Del Ben, V. V. Rybkin, P. Seewald, F. Stein, T. Laino, R. Z. Khaliullin, O. Schütt, F. Schiffmann, D. Golze, J. Wilhelm, S. Chulkov, M. H. Bani-Hashemian, V. Weber, U. Borštnik, M. Taillefumier, A. S. Jakobovits, A. Lazzaro, H. Pabst, T. Müller, R. Schade, M. Guidon, S. Andermatt, N. Holmberg, G. K. Schenter, A. Hehn, A. Bussy, F. Belleflamme, G. Tabacchi, A. Glöß, M. Lass, I. Bethune, C. J. Mundy, C. Plessl, M. Watkins, J. VandeVondele, M. Krack, and J. Hutter, J. Chem. Phys. **152**, 194103 (2020).
[5] M. Iannuzzi, J. Wilhelm, F. Stein, A. Bussy, H. Elgabarty, D. Golze, A.-S. Hehn, M. Graml, S. Marek, B. Sertcan Gökmen, C. Schran, H. Forbert, R. Z. Khaliullin, A. Kozhevnikov, M. Taillefumier, R. Meli, M. B. V. V. Rybkin and, R. Schade, O. Schütt, J. V. Pototschnig, H. Mirhosseini, A. Knüpfer, D. Marx, M. Krack, J. Hutter, and T. D. Kühne, J. Phys. Chem. B **130**, 1237 (2026).
[6] "CP2K Open Source Molecular Dynamics,".
[7] S. Ruiz-Barragan, D. Muñoz-Santiburcio, and D. Marx, J. Phys. Chem. Lett **10**, 329 (2019).
[8] S. Ruiz-Barragan, F. Sebastiani, P. Schienbein, J. Abraham, G. Schwaab, R. R. Nair, M. Havenith, and D. Marx, Phys. Chem. Chem. Phys. **24**, 24734 (2022).
[9] B. Das, S. Ruiz-Barragan, and D. Marx, J. Phys. Chem. Lett **14**, 1208 (2023).
[10] B. Das, S. Ruiz-Barragan, B. Bagchi, and D. Marx, Nano Lett. **24**, 15623 (2024).
[11] B. Hammer, L. B. Hansen, and J. K. Nørskov, Phys. Rev. B **59**, 7413 (1999).
[12] S. Grimme, J. Antony, S. Ehrlich, and H. Krieg, J. Chem. Phys. **132**, 154104 (2010).
[13] S. Goedecker, M. Teter, and J. Hutter, Phys. Rev. B **54**, 1703 (1996).
[14] C. Hartwigsen, S. Gœdecker, and J. Hutter, Phys. Rev. B **58**, 3641 (1998).
[15] M. Krack, Theor. Chem. Acc. **114**, 145 (2005).
[16] J. VandeVondele and J. Hutter, J. Chem. Phys. **127** (2007).
[17] S. Ruiz-Barragan, D. Muñoz-Santiburcio, S. Körning, and D. Marx, Phys. Chem. Chem. Phys. **22**, 10833 (2020).
[18] S. Ruiz-Barragan, H. Forbert, and D. Marx, Phys. Chem. Chem. Phys. **25**, 28119 (2023).
[19] W. Wagner and A. Pruß, J. Phys. Chem. Ref. Data **31**, 387 (2002).
[20] E. Carter, G. Ciccotti, J. T. Hynes, and R. Kapral, Chem. Phys. Lett. **156**, 472 (1989).
[21] M. Sprik and G. Ciccotti, J. Chem. Phys. **109**, 7737 (1998).
[22] M. Sprik, Chem. Phys. **258**, 139 (2000).
[23] D. Muñoz Santiburcio and D. Marx, Phys. Rev. Lett. **119**, 056002 (2017).
[24] M. Galib, T. T. Duignan, Y. Misteli, M. D. Baer, G. K. Schenter, J. Hutter, and C. J. Mundy, J. Chem. Phys. **146**, 244501 (2017).
[25] P. Montero de Hijes, C. Dellago, R. Jinnouchi, and G. Kresse, J. Chem. Phys. **161**, 131102 (2024).
[26] A. V. Bandura and S. N. Lvov, J. Phys. Chem. Ref. Data **35**, 15 (2006).